

Unraveling direct formation of hierarchical zeolite Beta by DLS, SAXS, liquid and Solid-State NMR: Insights at the supramolecular level

Maria Castro ¹, Pit Losch ^{1*}, Woojin Park ², Mohamed Haouas ³, Francis Taulelle ⁴, Claudia Loerbroks ¹, Gert Brabants ⁴, Eric Breynaert ⁴, Christine E. A. Kirschhock ⁴, Ryong Ryoo ², Wolfgang Schmidt ^{1*}

¹ *Max-Planck-Institut für Kohlenforschung, Mülheim an der Ruhr, Germany*

² *CNCR, Institute for Basic Science, Daejeon, Republic of Korea*

³ *Institut Lavoisier de Versailles, UVSQ, CNRS, Versailles, France*

⁴ *Center for Surface Chemistry and Catalysis, KU Leuven, Belgium*

Supporting Information

1. Experimental

1.1. Zeolite syntheses

The reactants used in all these syntheses were TEOS (Sigma Aldrich, 98%), TEOAH (Sigma Aldrich, 35 wt%), and $\text{Al}(i\text{-OBu})_3$ (Sigma Aldrich). $\text{N}_6\text{-diphe}(\text{OH})_6$ and $\text{N}_6\text{-diphe}(\text{Cl})_4(\text{Br})_2$ were synthesized according to published procedure.¹

Typical zeolite synthesis conditions were as follows:

The sample **nano-Beta_{sol}** was prepared with the following molar ratios $x \text{ SiO}_2 : 0.033 \text{ Al}_2\text{O}_3 : 0.06 \text{ N}_6\text{-diphe}(\text{OH})_6 : 300 \text{ H}_2\text{O} : 4/x \text{ EtOH} : 0.2 \text{ i-PrOH}$ ($x = 0.12, 0.24, 0.36, 0.72, 1$). All reactants were premixed while TEOS was introduced dropwise as last component. The resulting synthesis mixture was left stirring for 24 h to allow complete hydrolysis of TEOS. The aged clear synthesis solution was transferred into a Teflon lined stainless steel autoclave and hydrothermally treated at 140°C for times up to five days under static conditions. The exact composition of the clear solution studied in more detail by DLS, SAXS and NMR, was: $1 \text{ SiO}_2 : 0.033 \text{ Al}_2\text{O}_3 : 0.06 \text{ N}_6\text{-diphe}(\text{OH})_6 : 300 \text{ H}_2\text{O} : 4 \text{ EtOH} : 0.2 \text{ i-PrOH}$.

The sample **nano-Beta_{gel}** was prepared with the following molar ratios $1 \text{ SiO}_2 : 0.033 \text{ Al}_2\text{O}_3 : 0.033 \text{ N}_6\text{-diphe}(\text{Cl})_4(\text{Br})_2 : 0.22 \text{ Na}_2\text{O} : 53 \text{ H}_2\text{O} : 4 \text{ EtOH} : 0.2 \text{ i-PrOH}$. All reactants were premixed and TEOS added at once. Its hydrolysis was guaranteed by homogenizing the mixture for 1 h with a vortex stirrer. Then, the resulting gel was aged for 6 h at 60°C. The aged dense gel was transferred into a Teflon lined stainless steel autoclave and a hydrothermal synthesis was performed at 140°C for varying times up to 7 days under tumbling conditions.

A conventional zeolite, denoted as **conv. Beta_{TEAOH}** in Fig S13, was synthesized from a clear solution with composition $1 \text{ SiO}_2 : 0.02 \text{ Al}_2\text{O}_3 : 0.5 \text{ TEOAH} : 16 \text{ H}_2\text{O} : 4 \text{ EtOH}$. In a first step the Al source (aluminum tri-sec-butoxide), water, and tetraethylammonium hydroxide (TEAOH) were mixed and stirred for 1 h. Then the Si source (tetraethyl orthosilicate, TEOS) was added dropwise under mild stirring. The resulting sol was kept stirring to allow slow hydrolysis of TEOS (24 h). The final clear sol was transferred into a Teflon-lined autoclave and heated at 140°C for 5 days. The autoclave then was removed from the oven and quenched to room temperature. Separation of the solid from the mother liquor was achieved by centrifugation in a Sartorius Sigma 3K30 centrifuge.

1.2.Characterization

Textural properties were studied with argon sorption experiments on a 3Flex from Micromeritics for the nano-Beta_{gel} and nano-Beta_{sol} sample. They have been outgassed and dehydrated at 623 K for 8 h under vacuum. Then argon adsorption was measured at 87 K (liquid Ar). Sorption measurements for other samples have been carried out conventionally with nitrogen at 77 K. Apparent specific surface areas were calculated with the B.E.T. model using data in the relative pressure range of 0.05 to 0.3. Calculation of pore size distributions and pore volumes was performed using the NLDFT method with models assuming sorption of argon in cylindrical pores in oxidic materials at 87 K using the Micromeritics 3Flex software package. Total pore volumes were calculated from the volume adsorbed at relative pressures of $p/p_0 = 0.99$.

DLS measurements were performed with an ALV/CGS-3 instrument (ALV, Langen, Germany). Prior to analyses, the samples were filtered with 200 nm CHROMAFIL PTFE syringe filters. DLS measurements were performed at scattering angles of 30°, 90° and 150° using a laser with a wavelength of 632.8 nm.

SAXS experiments were performed with an Anton Paar SAXSess mc² instrument (Kratky camera) with line-collimated CuK_α radiation. The liquids containing the reaction mixtures were measured in sealed 1 mm quartz glass capillaries (wall thickness 0.01 mm) on a temperature-controlled TCS 120 stage (Anton Paar). The scattered intensities were recorded with a 2D CCD camera (Princeton Instruments). Prior to data analysis, conventional data processing included subtraction of electronic background (CCD camera), scattering background from solvent and capillary and desmearing of the scattering curve (accounting for axial divergence due to measurement in capillaries). The data analysis was then performed with the SANS and USANS Analysis Tools for Igor Pro provided by the NIST Center for Neutron Research.² Scattering lengths densities for the individual phases have been calculated using the SasView 3.1.0 software package.³

XRD data were measured with a Stoe STADI P transmission diffractometer in Debye–Scherrer geometry. The instrument was equipped with a bent secondary germanium monochromator allowing measurements with monochromatic CuK_{α1} radiation. Diffracted intensities were recorded with a position-sensitive detector (PSD) fabricated by Stoe. The PSD enables simultaneous recording of about 6° 2θ. Samples were measured in 0.7 mm glass capillaries (wall thickness 0.01 mm) either in aqueous suspensions or as dry powders after separation of the nanoparticles by ultracentrifugation.

²⁷Al, ²⁹Si, ¹⁴N, and ¹H liquid-state NMR measurements were performed in 10 mm quartz tubes using a Bruker AVANCE-500 spectrometer for ²⁷Al and ²⁹Si, and Bruker AVANCE 400 spectrometer for ¹⁴N and ¹H. The ²⁷Al NMR spectra were recorded at a ²⁷Al frequency of 130.33 MHz with a $\pi/12$ rad pulse length of 2.1 μs, a recycle delay of 0.1 s, and acquisition 1024 pulse transients. The ²⁹Si NMR spectra were

obtained at a ^{29}Si frequency of 99.35 MHz with a $\pi/4$ rad pulse length of 3.7 μs , a recycle delay of 7 s, and acquisition of 1024 pulse transients. The ^1H NMR spectra were recorded at a ^1H frequency of 400.13 MHz with a $\pi/2$ rad pulse length of 30.0 μs , a recycle delay of 4 s, and acquisition of 16 pulse transients. The ^{14}N NMR spectra were obtained with a Larmor frequency of 28.91 MHz under proton decoupling using a $\pi/10$ rad pulse length of 6.2 μs , a recycle delay of 2 s, and 1024 scans. Translational diffusion measurements were performed using Bruker's "ledbpgs2s" stimulated echo DOSY pulse sequence including bipolar and spoil gradients.

All MAS NMR spectra were recorded on a Bruker Avance 500 spectrometer at a resonance frequency of 500.1 MHz for ^1H , 130.3 MHz for ^{27}Al , 125.7 MHz for ^{13}C , and 99.3 MHz for ^{29}Si . The samples were packed in a 4 mm zirconia rotor, and were spun at 10 kHz. For the ^1H MAS NMR spectra 8 scans were recorded with a recycle delay of 5 s and a $\pi/2$ rad pulse of 4.1 μs . The $^{13}\text{C}\{^1\text{H}\}$ cross-polarization (CP) MAS NMR spectra were recorded using a 2.5 ms contact time, 2 s recycle delay and ^1H SPINAL-64 decoupling. 1024 transients were accumulated. For the $^{13}\text{C}\{^1\text{H}\}$ HETCOR MAS NMR spectrum, the contact time was set to 1.5 ms, and 128 t_1 slices with 112 transients each were recorded with recycle delay of 5 s. The $^{29}\text{Si}\{^1\text{H}\}$ CPMAS NMR spectra were recorded using a 6.5 ms contact time, 1.5 s recycle delay and 2048 transients. For the quantitative single-pulse ^{29}Si MAS NMR spectra, 136 scans were recorded with a recycle delay of 250 s and a $\pi/2$ rad pulse of 4.4 μs . The $^{29}\text{Si}\{^1\text{H}\}$ HETCOR MAS NMR spectrum was recorded with a contact time of 6 ms, 16 t_1 slices with 1024 transients, and a recycle delay of 5 s. For ^{27}Al NMR, MAS spectra were recorded with signal averaging for 1024 transients with a repeat interval of 0.1 s. The ^{27}Al MQMAS spectra were recorded using a three-pulse sequence for triple-quantum generation/reconversion and z -filtering with signal averaging for 196 transients for each of 128 t_1 increments of 25 μs . All two-dimensional NMR spectra were recorded using the States procedure to obtain phase sensitive spectra.

All NMR measurements were performed with the natural abundance of the measured element. The ^{27}Al and ^{14}N chemical shifts are reported relative to $\text{Al}(\text{H}_2\text{O})_6^{3+}$ and nitromethane, respectively, and the ^{29}Si , ^{13}C and ^1H chemical shifts are referenced to tetramethylsilane (TMS). Decomposition and simulation of the NMR spectra were achieved using the *NMRnotebook* program.⁴

HR-SEM images were measured with a Hitachi S-5500 high-resolution scanning electron microscope with an acceleration voltage of 30 kV. Samples were placed on copper grids with 3 nm carbon coatings.

1.3. Modeling

Charmm General Force Field V. 2b6 for modeling of the surfactant and the TIP3P model for explicit solvent simulations have been used in this work. The model so far includes one surfactant (N₆-diphe, 285 atoms) included in a water box of 102*102*102 Å (101129 water molecules). For the simulation, the system was minimized, heated to 300 K and equilibrated for 5 ns using Langevin dynamics and a Langevin piston barostat. The simulations were performed with the NAMD program. A force field consists of parameters for different atoms and molecules, which can be used to calculate the potential energy of systems. The total energy consists of bonded (bond, angle and dihedral modeled as harmonic oscillators or as a Morse potential) and non-bonded (electrostatic and van der Waals modeled with a Lennard-Jones potential and Coulombs law) terms. These parameters are obtained by fitting the values to experimental data and *ab initio* calculations. The example used is an isobaric-isothermic one (NPT), and the pressure, which is 1 atm.

2. Supplementary Results

Table S1. Properties of materials investigated in this work.

Samples	Si/Al ^a	Si/Al ^b	T (°C)	SDA
nano-Beta _{sol}	16.7	12.3	140	N ₆ -Diphe (OH) ₆
nano-Beta _{gel}	16.7	15.4	140	N ₆ -Diphe (Cl) ₄ (Br) ₂

a: Si/Al-ratio of the synthesis gel.

b: Si/Al-ratio of the final product, by ICP.

The Molecular Structure of N₆-diphe

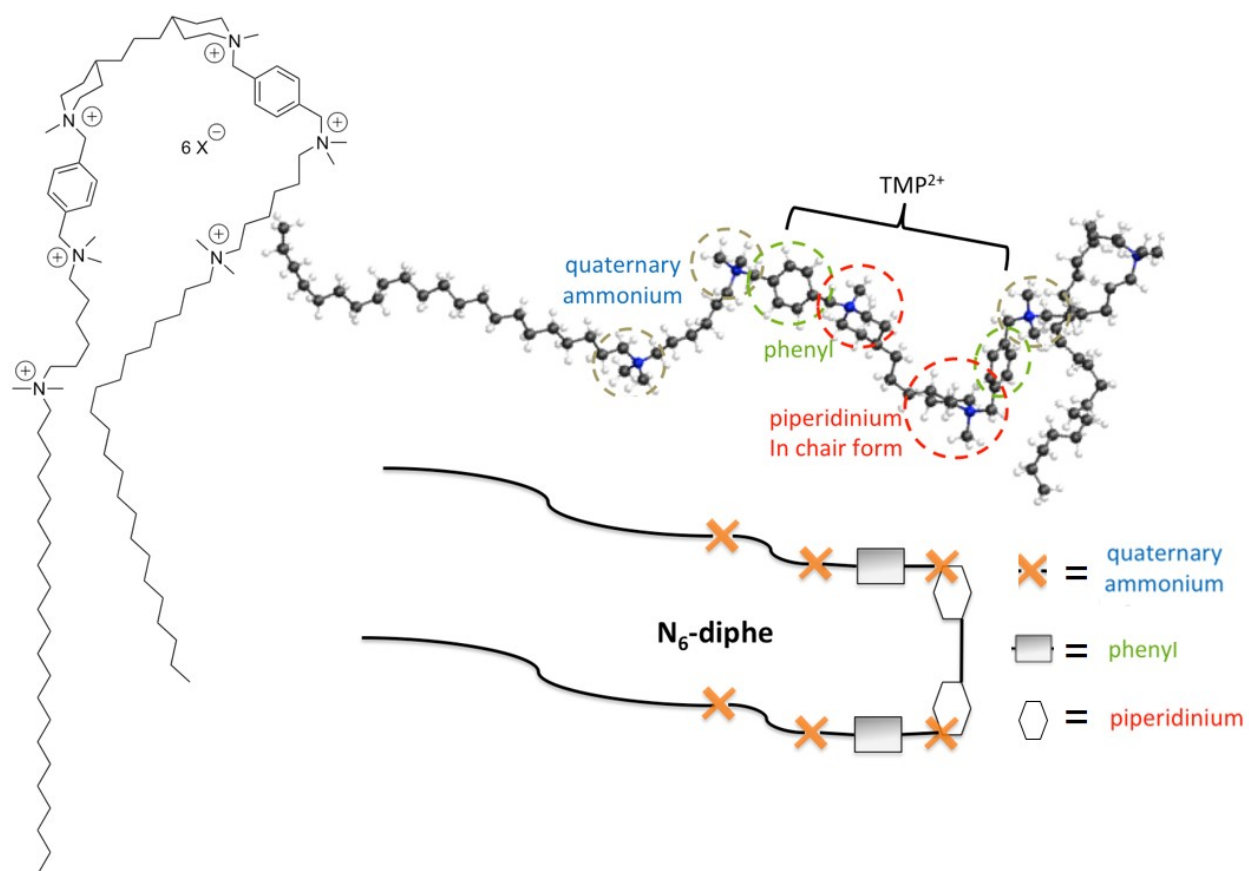


Figure S1. Various structural representations of the studied gemini-type piperidine-based multi-ammonium surfactant denoted as N₆-diphe(X)₆ with X⁻ being either OH⁻, Cl⁻ or Br⁻. A similar SDA with the structure denoted as TMP²⁺ in the structure above has been used by Hould et al. for the synthesis of aluminum-free zeolite Beta (ref. 41).

2.1. Results from Molecular Dynamics Calculations

For describing the dynamical behavior of SDA we have used classical molecular dynamics (MD) within the NAMD program suite⁵ using the Charmm General Force Field V. 2b6.⁶ In our computations, one SDA molecule was considered in a 100 Å long cubic box together with 34,647 water molecules and 6 chloride ions. In the experiment hydroxyl groups balancing these charges but chloride atoms were included in the simulation since they are better explored than hydroxyl ions in molecular dynamics. Periodic boundary conditions were achieved with the Particle Mesh Ewald method. A cut-off distance of 10 Å was used for non-coulombic interactions.

The system was equilibrated to reproduce experimental conditions of 1 atm and temperature of 413 K with Langevin dynamics and Nosé-Hoover Langevin piston pressure control. A time step of 2 fs together with rigid bonds for water were used. After minimizing and heating the system, the simulation was propagated for 400 ns in NVT ensemble. After 400 ns, the 413 K simulation is well converged according to our criteria.

The probability of conformations and the free energy differences between the conformations were estimated with the direct counting method.⁷

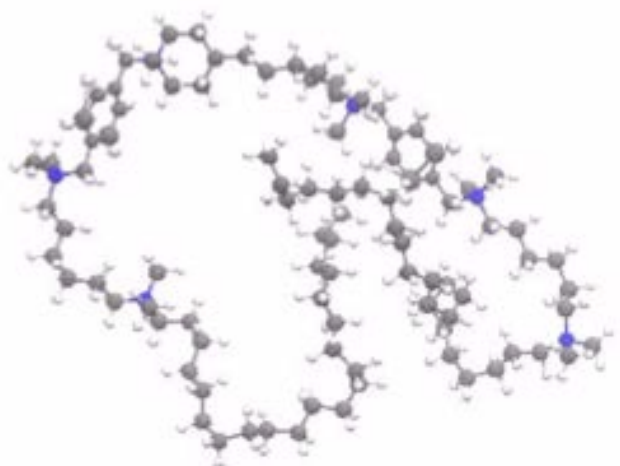


Figure S2. Classical molecular dynamics simulation showed motion and conformations of the template molecule in an aqueous solution. One N_6 -diphe⁶⁺ cation in a Charmm Force Field with 34647 H₂O and 6 Cl⁻ anions. (A movie showing the motion of the N_6 -diphe molecule in water and 6 Cl⁻ anions is available as additional supporting information.)

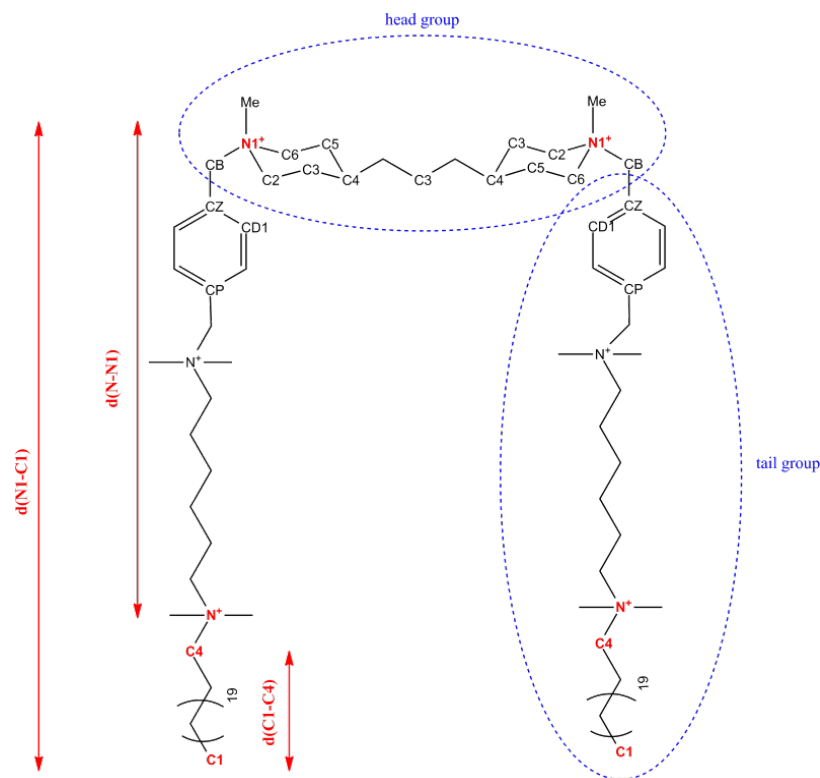


Figure S3. Structure of the N_6 -diphe $^{6+}$ molecule and important distances.

Of special interest for the experiment are the lengths of the tails ($d(N1-C1)$) in the SDA (**Figure S3**). Whereas the head group is said to be attached to the silicate, the tails are free to move and might act as a buffer between the formed zeolite particles. Therefore, the different conformations of these tails were investigated computationally. The overall distribution of different tail length can be seen in **Figure S4**.

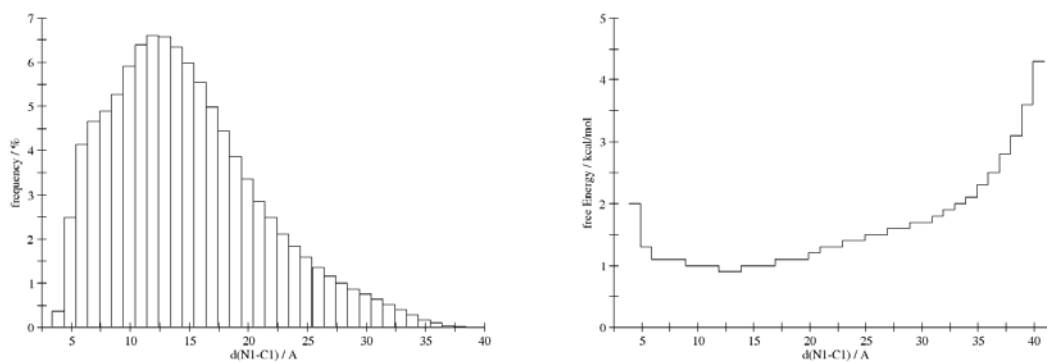


Figure S4. Distribution of probability (left) and relative free energy (right) at different $N1-C1$ distances at 413 K.

The tails are very flexible reaching $N1-C1$ distances from 4 to 40 Å. Values of 10 to 16 Å have the highest probability with 43% of all possible $N1-C1$ conformations. The minimum of free energy is at 12 to 14 Å. Examples for structures can be seen in **Figure S5**. At the energetically low conformations the chain interacts with itself, with the $C1-C4$ chain coiled around itself or the $N-N1$ chain.

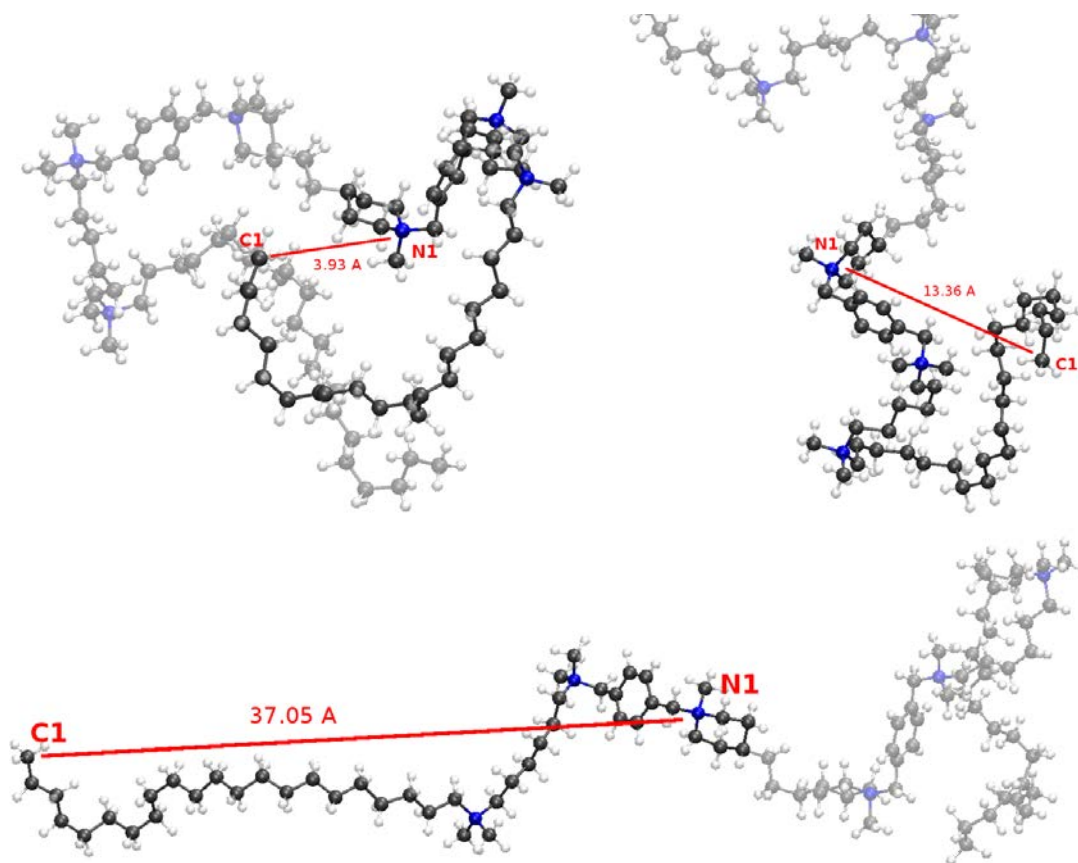


Figure S5. Examples for three different N1-C1 distances at 413 K. Water molecules are omitted for clarity.

The N1-C1 distance can be separated in two parts (**Figure S6**): The distances C1-C4 and N1-N4 reach from 3 to 25 Å and have maxima at 15-19 Å with 42% as well as 6 Å with 2% probability. $d(\text{N1-N})$ is shorter with 6 to 17 Å and has one maximum at 10-13 Å with 55% and a smaller one at 15 Å with 4% probability. The conformations within one tail are not correlated with each other; this shows the high flexibility within the single tails.

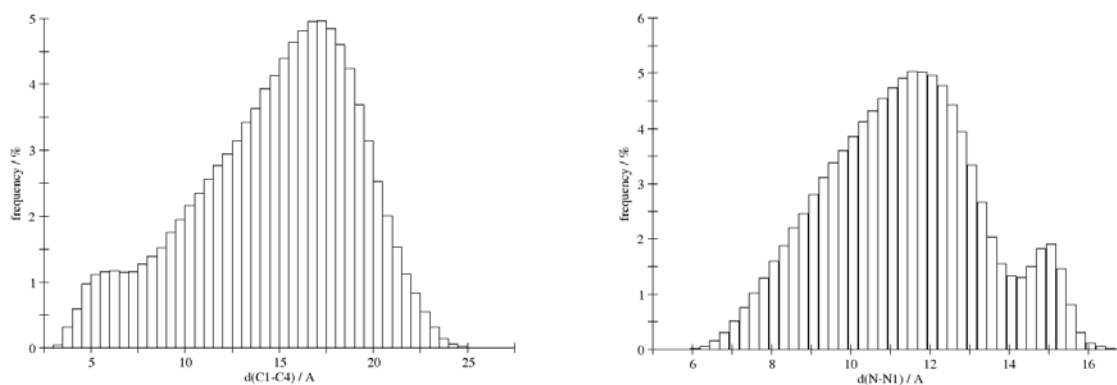


Figure S6. Distribution of the C1-C4 (left) and N-N1 distances (right) at 413 K.

2.2 Results from Dynamic Light Scattering

Si/OH=2.77

30 SiO₂ :1 Al₂O₃:1.8 SDA(OH)₆ :9000 H₂O: 120 EtOH: 6 i-PrOH

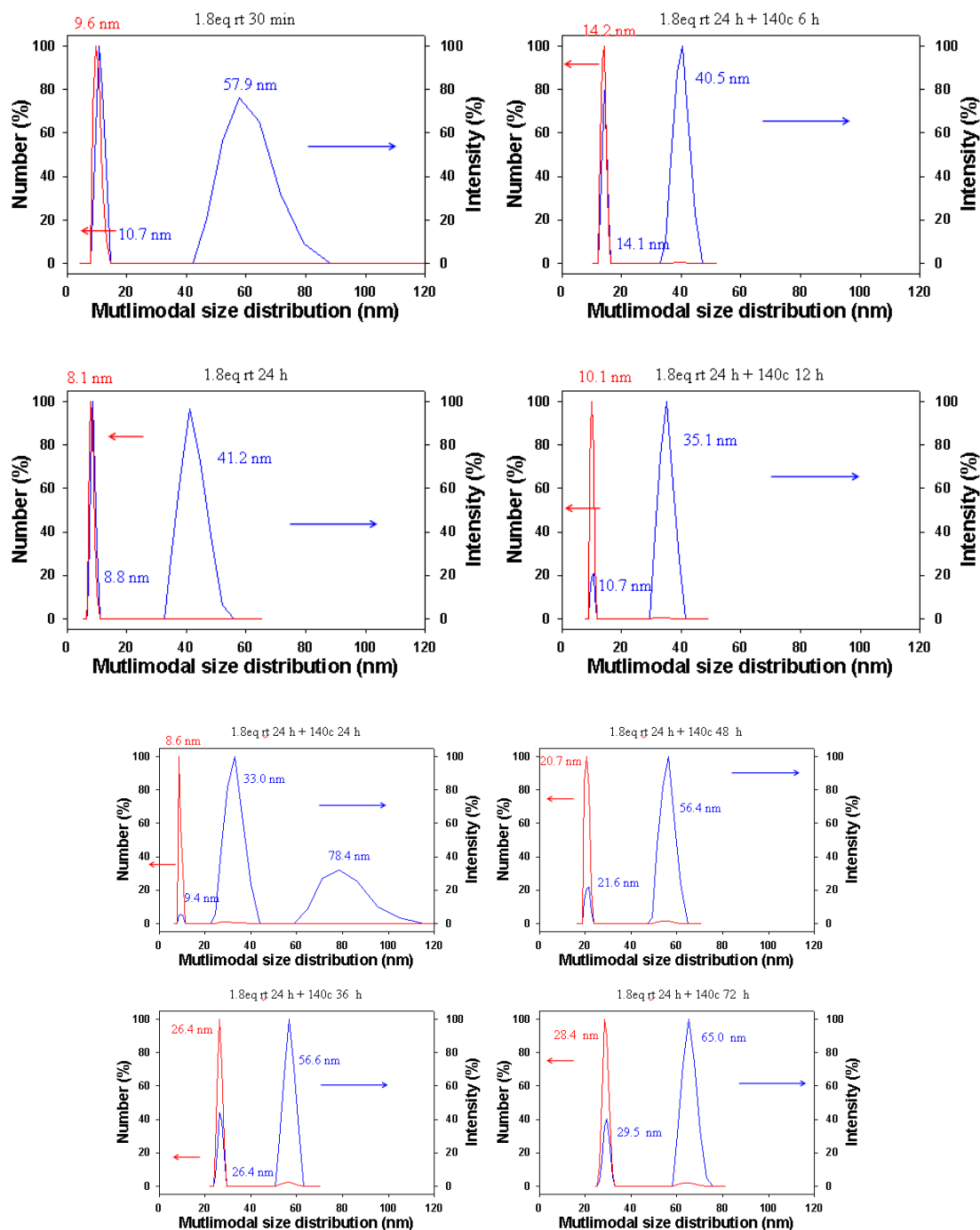


Figure S7. Particle size distribution for nano-Beta_{sol} at Si/OH ratio of 2.77 from DLS data.

Table S2. DLS data for the synthesis of nano-Beta_{sol}: The evolution of a clear light yellow solution from aging (A) to the hydrothermal synthesis (HTS). (Data extracted from **Figure S7**)

	T (°C)	t (h)	pH	Particle-size (nm)
A	20	0.5	10	9.6
A	20	24	10	8.1
HTS	140	24 + 6	10	14.1
HTS	140	24 + 12	10	10.1
HTS	140	24 + 24	10	8.6
HTS	140	24 + 36	11	26.4
HTS	140	24 + 48	11	20.7
HTS	140	24 + 72	10	28.4

2.3. Results from Small Angle X-ray Scattering and X-ray Diffraction

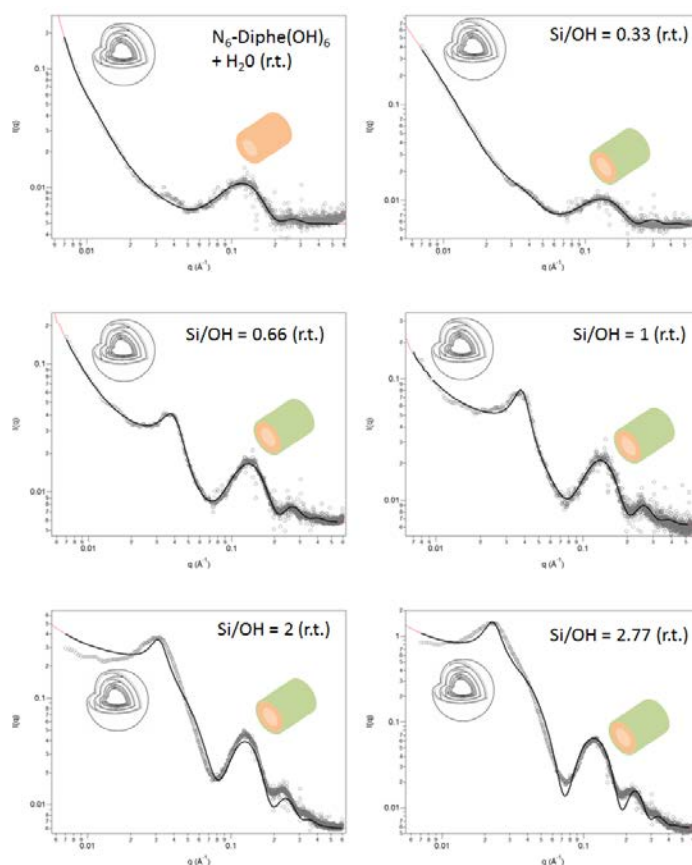


Figure S8. Experimental SAXS data and calculated intensities as obtained by fitting different models (see **Table S3**) to data measured for nano-Beta_{sol} during aging at room temperature and upon heating at 140°C. The curves of the samples with higher silicate content (Si/OH = 2 and 2.77) show some deviation of the fit from the measured data which could be caused by interference effects due to scattering from particles in close proximity. The curves are fitted with two models considering cylindrical core-shell particles (consecutive maxima and minima) and multilamellar paracrystals (Gaussian peak and high intensity at lower q). The ranges which are mainly affected by one of the two models are indicated by the sketched vesicles and the core-shell cylinders. The results from the fitting of the sum models are reported in **Table S3**.

Table S3. Results from SAXS data of sols for nano-Beta_{sol} after mixing of all components and hydrolysis of TEOS at room temperature fitted with summed *polyCoShCyl* and *LamParaCryst* models.

Si/OH	r_c core [nm]	L_c cylinder [nm]	th_s silica shell [nm]	th_L lamellae [nm]	d_L inter-lam. [nm]	N₆-diphe in core [%]
0.33	2.0 (0.16)	6.4	0.35	6.4	13.1 (3.28)	11
0.66	2.2 (0.22)	4.4	0.51	6.8	14.4 (4.03)	14
1.00	2.2 (0.22)	4.7	0.64	6.5	15.6 (3.43)	16
2.00	2.3 (0.25)	6.1	0.97	5.9	18.9 (4.35)	18
2.77	2.4 (0.19)	9.5	1.07	7.2	26.0 (6.24)	21

r = radius of the core of the core-shell cylinders, L = lengths of core-shell cylinders, th_s = thickness of the silica shell in the core-shell cylinders, th_L = thickness of the lamellae in lamellar paracrystals, d_L = distance between adjacent lamellae in lamellar paracrystals, N₆-diphe in core = maximum percentage of N₆-diphe that can be accommodated in the cores of cylindrical core-shell particles (estimated by assuming all aluminosilicate to be located in the shells with given thickness and inner radius (= r_c) which results in a maximum volume for the core that could be filled with N₆-diphe. Specific densities for the components were assumed as follows: silica 2.2 cm³.g⁻¹, alumina as 3.95 cm³.g⁻¹, organic core 0.8 cm³.g⁻¹). In order to simplify the modeling, the silicate shell on the faces of the cylinders was set as infinitely thin. The numbers in brackets report the standard deviations (σ) to the respective mean values.

Table S4. Refined parameters used for fitting of the SAXS data of sols for nano-Beta_{sol} after mixing of all components and hydrolysis of TEOS at room temperature (Table S3).

	polyCoShCyl			LamParaCryst		
Si/OH	back-ground	radial poly-dispersity	scaling factor	back ground	poly-dispersity of spacing	scaling factor
0.33	5.50 e-3	0.08	1.036 e-3	0	0.25	3.536 e-3
0.66	5.61 e-3	0.10	1.48e e-3	0	0.28	2.427 e-3
1.00	6.00 e-3	0.10	1.481 e-3	0	0.22	1.542 e-2
2.00	6.00 e-3	0.11	1.630 e-3	0	0.23	3.178 e-2
2.77	6.29 e-3	0.08	1.855 e-3	0	0.24	7.927 e-2

The SLD for core (*polyCoShCyl*) and layer (*LamParaCryst*) were set to 6.84 e-6, the SLD for the shell (*polyCoShCyl*) was set to 1.715 e-5, the SLD for the solvent (*polyCoShCyl* and *LamParaCryst*) was set to 9.47 e-6. Face shell thickness (*polyCoShCyl*) was set to 1 e-10.

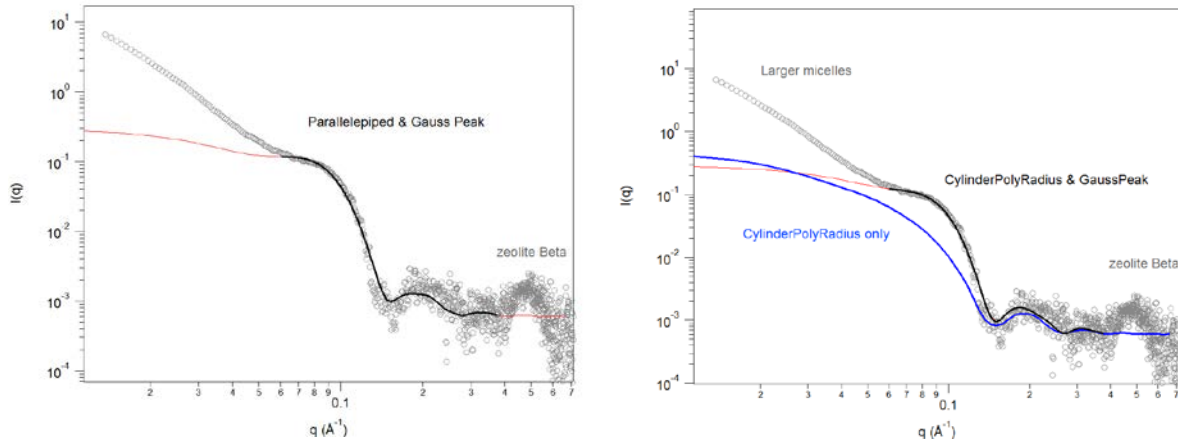


Figure S9. Experimental SAXS data and calculated intensities as obtained by fitting different models of the nano-Beta_{sol} sample obtained after 24 h at 140°C. The experimental curve can be fitted either with a model for a parallelepiped with dimensions of 4.7 x 4.7 x 14 nm (left) or with one for a cylinder with diameter of 5.2 nm and length of 9.5 nm (right). For both models a Gaussian peak must be considered in addition to the curve from the nanoparticles. The blue curve in the right figure shows the scattering of only the cylindrical particles, clearly indicating that a Gaussian peak must be considered which corresponds to a distance of about 8 nm. At low q values a third component adds to the scattering intensity, likely larger particles or aggregates consisting of smaller objects. A fourth component to the scattering curve is observed as a peak at a $q = 0.5\text{-}0.6 \text{ \AA}^{-1}$, corresponding to the first broad reflection of crystalline zeolite Beta. From the SAXS profiles shown above one cannot derive whether the elongated particles have the shape of cylinders or of parallelepipeds. Fits for both models were equally good. For simplicity cylindrical shape was thus assumed.

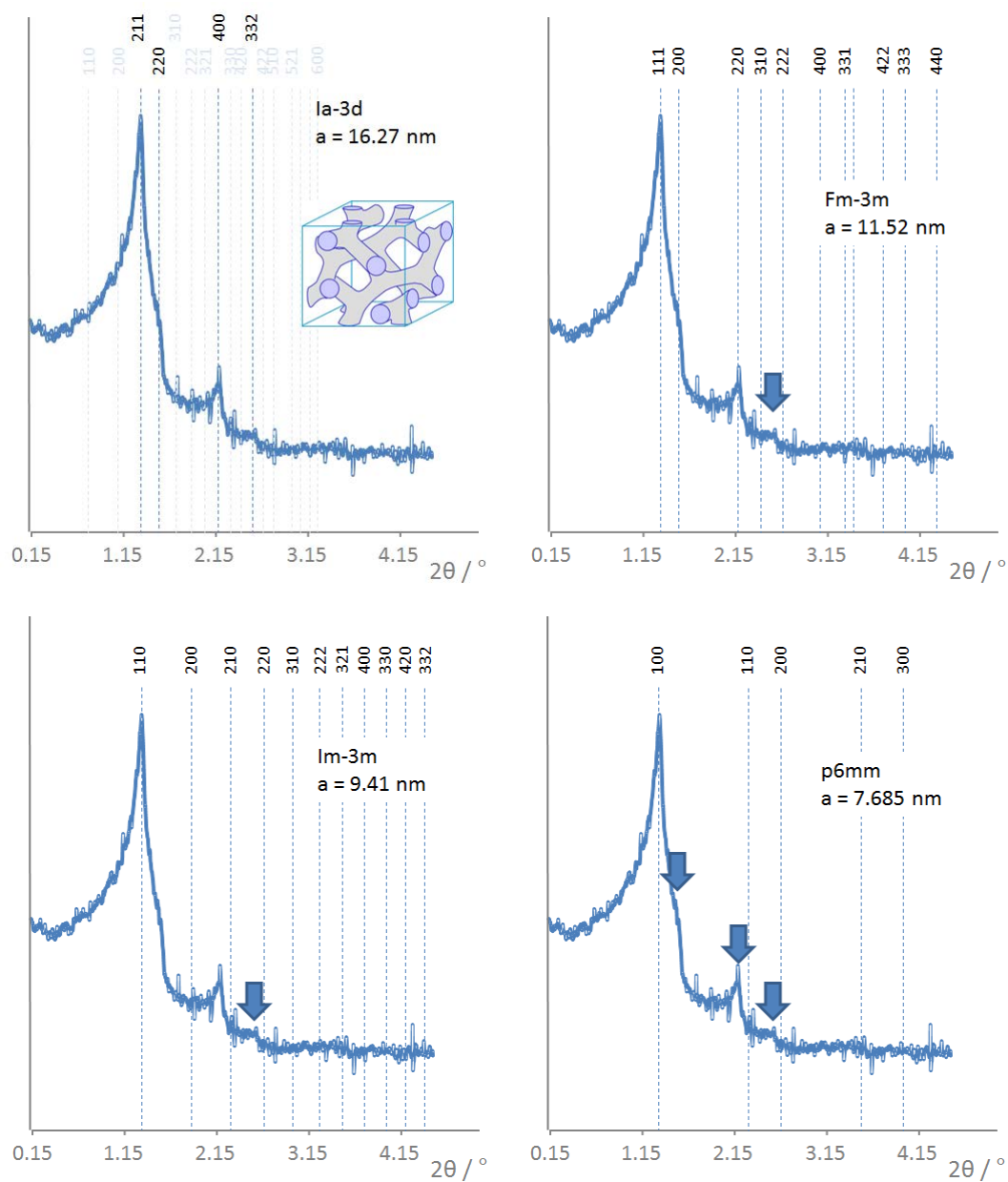


Figure S10. SAXS data evidence cubic geometry of objects observed in the reaction mixture for the synthesis of nano-Beta_{gel} prior to addition of TEOS. The pattern fits best to the Ia-3d symmetry, for all other cubic or hexagonal symmetries, some reflections cannot be indexed (arrows). The Ia-3d symmetry corresponds to that of the bi-continuous micellar system as observed during the formation of MCM-48 or KIT-6 silica (see inset).

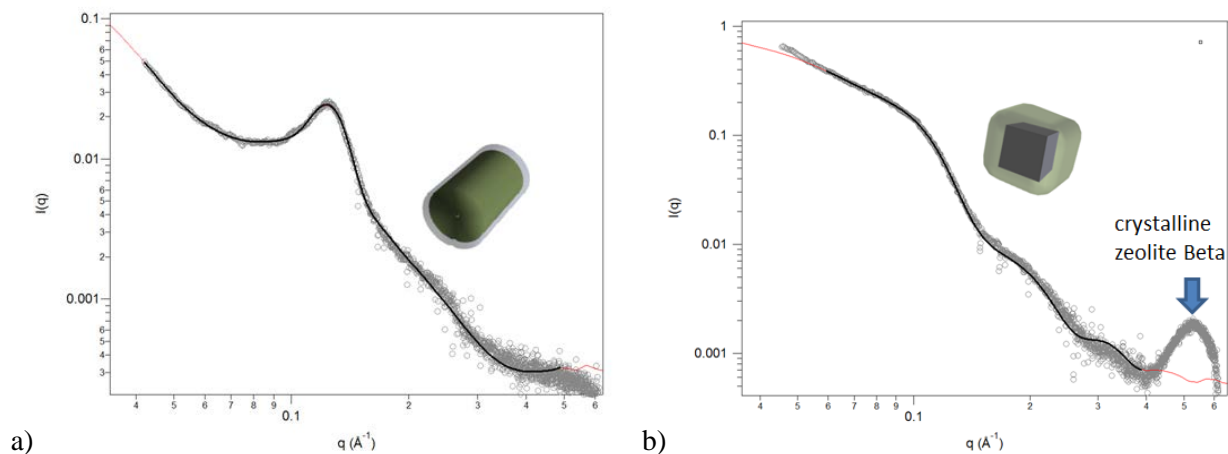


Figure S11. SAXS curves of nano-Beta_{gel} after a) aging at 60°C for 1 h and b) after hydrothermal reaction for 7 d. The curve in a) is fitted with a summed *polyCoShCyl* and *GaussPeak* model and the curve in b) with a summed *CylPolyRadius* and *GaussPeak* model.

Table S5. Results from SAXS data of nano-Beta_{gel} after mixing of all components and hydrolysis of TEOS at 60°C for 1h fitted with summed *polyCoShCyl* and *GaussPeak* models (first two rows) and after hydrothermal synthesis at 140°C fitted with summed *CylPolyRadius* and *GaussPeak* models (third and fourth row).

Si/OH	r_c core [nm]	L_c core [nm]	th_s silica shell [nm]	d_G Gauss peak [nm]	N_6 -diphe in core [%]
0.27	2.2	16.2	1.55	5.07	25.9
Si/OH	r_c cylinder [nm]	L_c cylinder [nm]	-	d_G Gauss peak [nm]	-
0.27	3.8	5.0	-	6.73	-

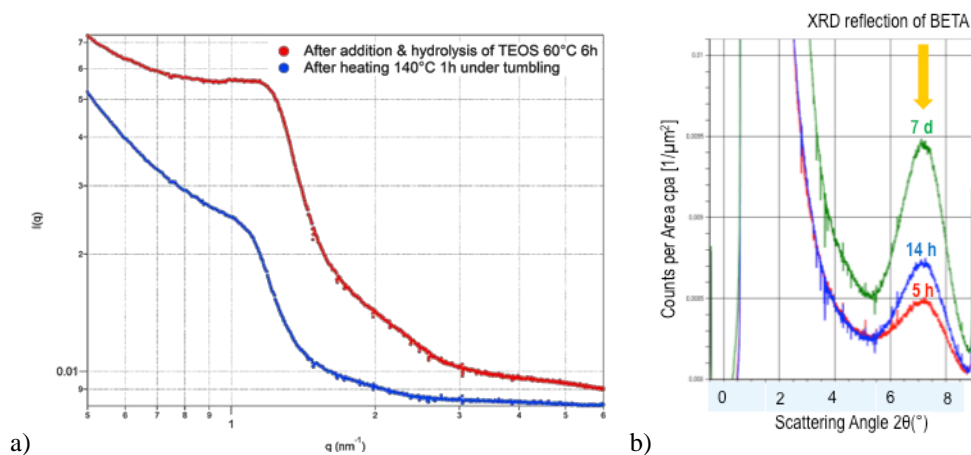


Figure S12. a) SAXS of the synthesis-gel of nano-Beta_{gel} containing aluminum: gel before hydrothermal synthesis (red), and a sample after 1 h under hydrothermal synthesis conditions. b) At prolonged synthesis conditions (5 h red, 14 h blue and 7 days in green), crystalline zeolite nano-Beta_{gel} is observed in the low angle X-ray diffraction.

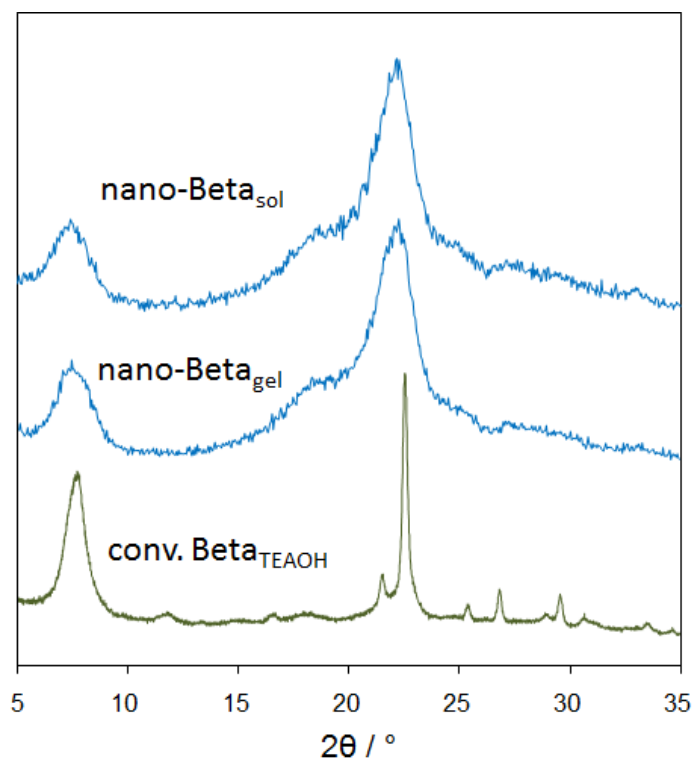


Figure S13. XRD patterns of nano-Beta_{sol} and nano-Beta_{gel} in comparison to a XRD pattern of conventional zeolite Beta synthesized with TEAOH as structure-directing agent at 140°C. Significant reflection broadening is caused by the nanoscopic sizes of the nano-Beta materials as compared to the reflections observed for the conventional zeolite Beta. The broader reflection which are visible in the pattern of the conventional zeolite Beta are caused by stacking disorder as typical for that zeolite.

2.4. NMR-results

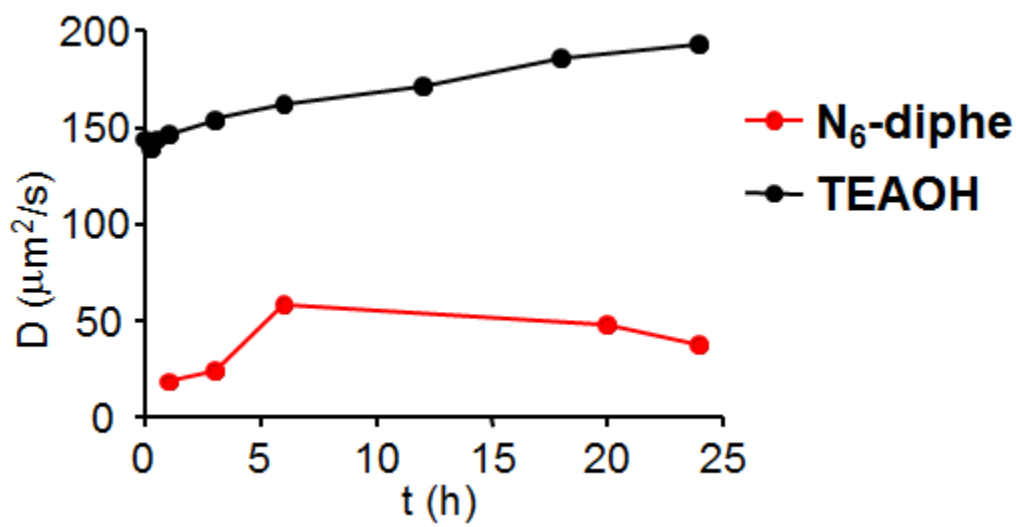


Figure S14. Evolution of diffusion coefficient of $\text{N}_6\text{-diphe}$ in synthesis medium of nano- Beta_{sol} (red) and colloidal zeolite Beta (black) (ref. 34) as measured by DOSY NMR at different hydrothermal treatment time.

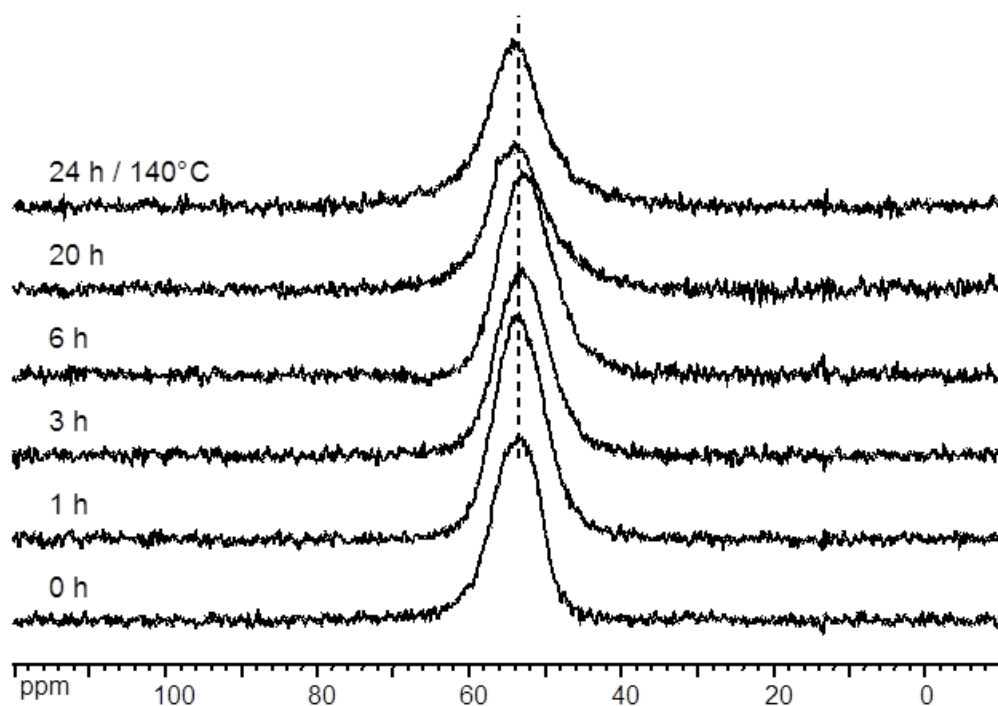


Figure S15. Evolution of ^{27}Al NMR spectra of synthesis medium of nano- Beta_{sol} at different hydrothermal treatment time.

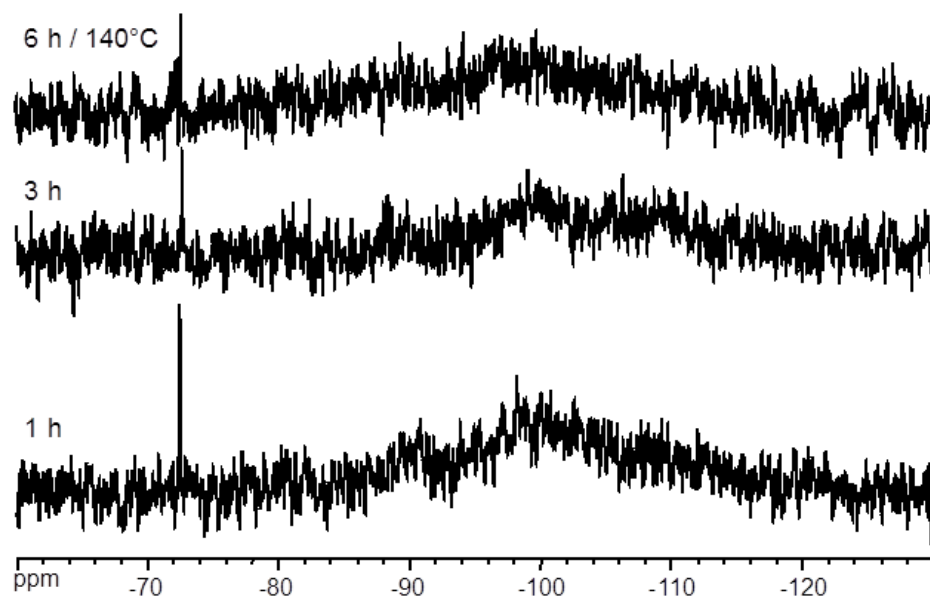


Figure S16. Evolution of ^{29}Si NMR spectra of synthesis medium of nano-Beta_{sol} at different hydrothermal treatment time.

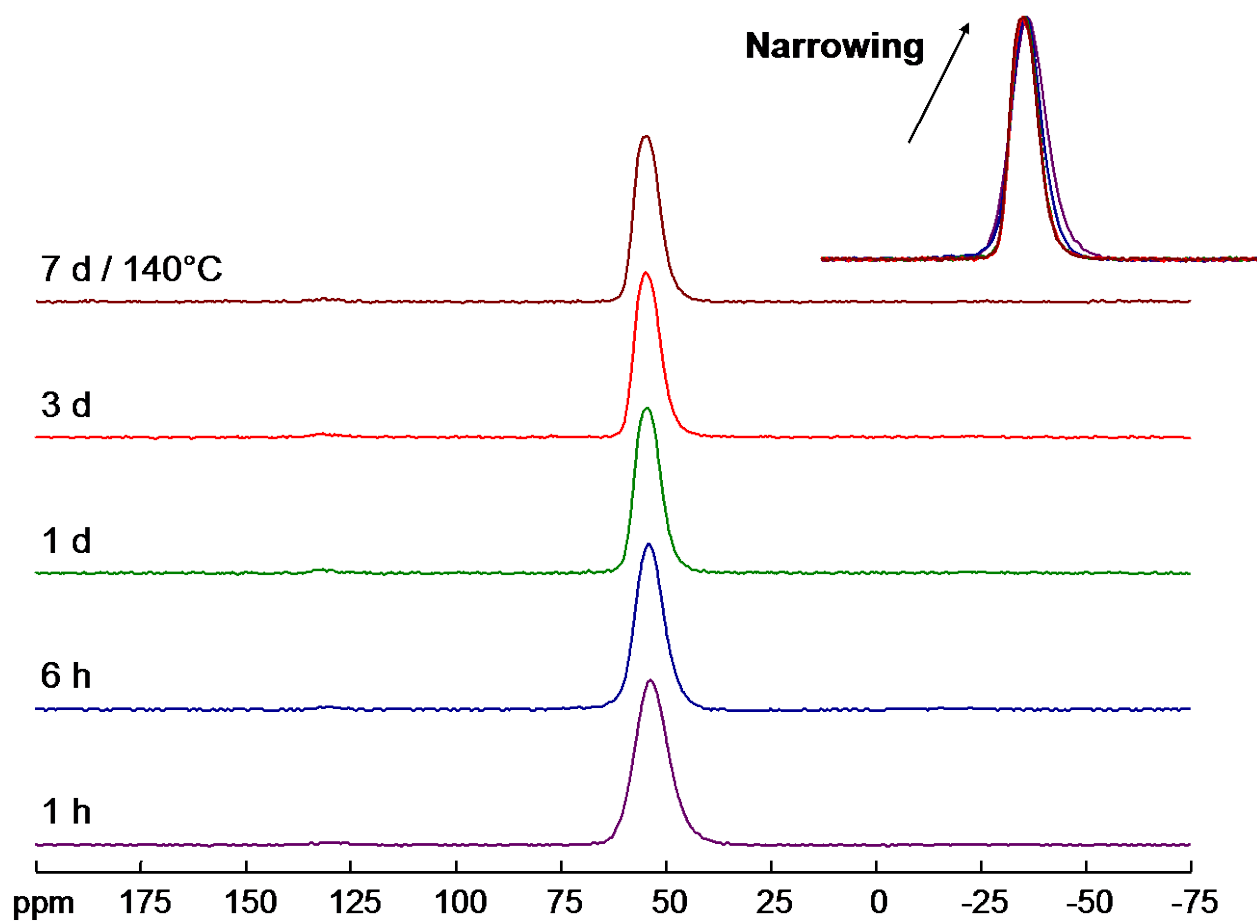


Figure S17. Evolution of solid-state ^{27}Al MAS NMR spectra of recovered solids from the synthesis of nano-Beta_{gel} at different hydrothermal treatment time.

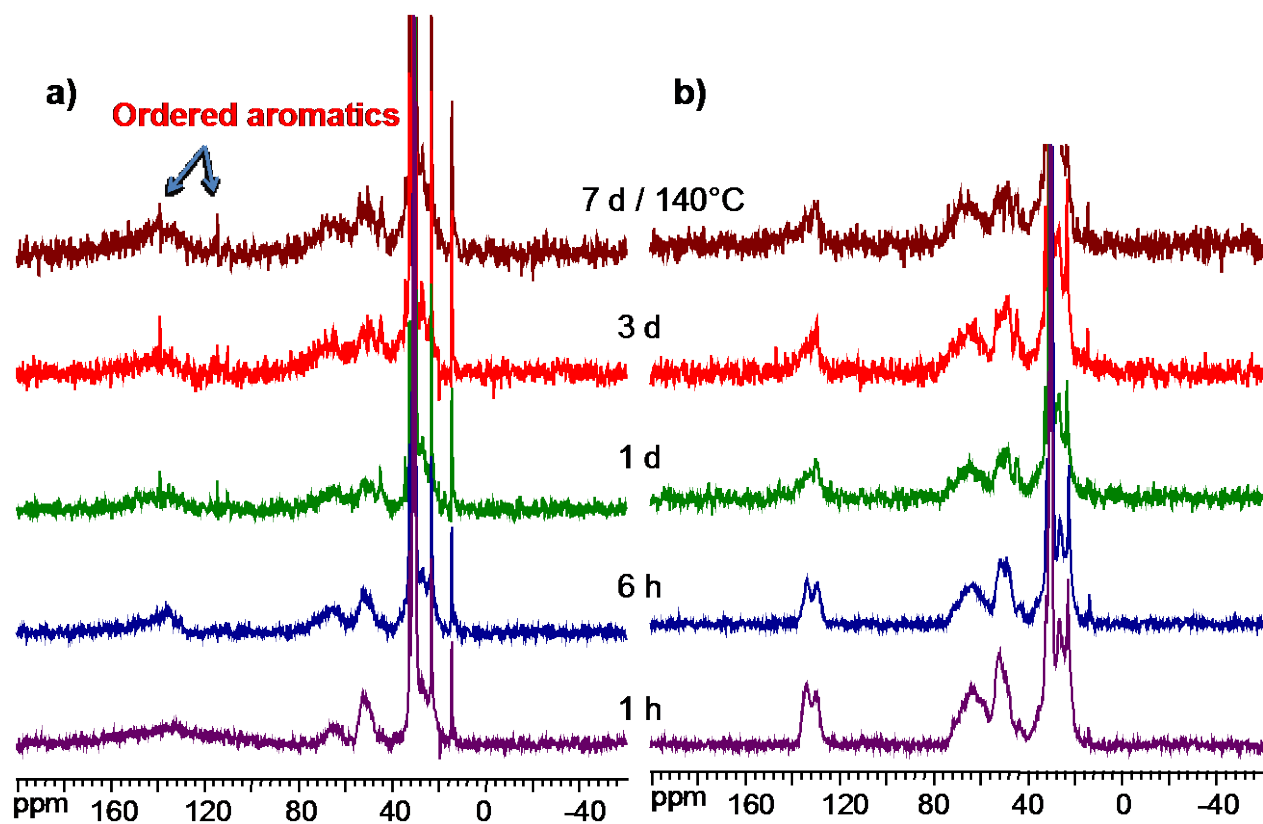


Figure S18. Evolution of solid-state $^{13}\text{C}\{^1\text{H}\}$ MAS NMR spectra of recovered solids from the synthesis of nano-Beta_{gel} at different hydrothermal treatment time: a) direct polarization; b) cross-polarization.

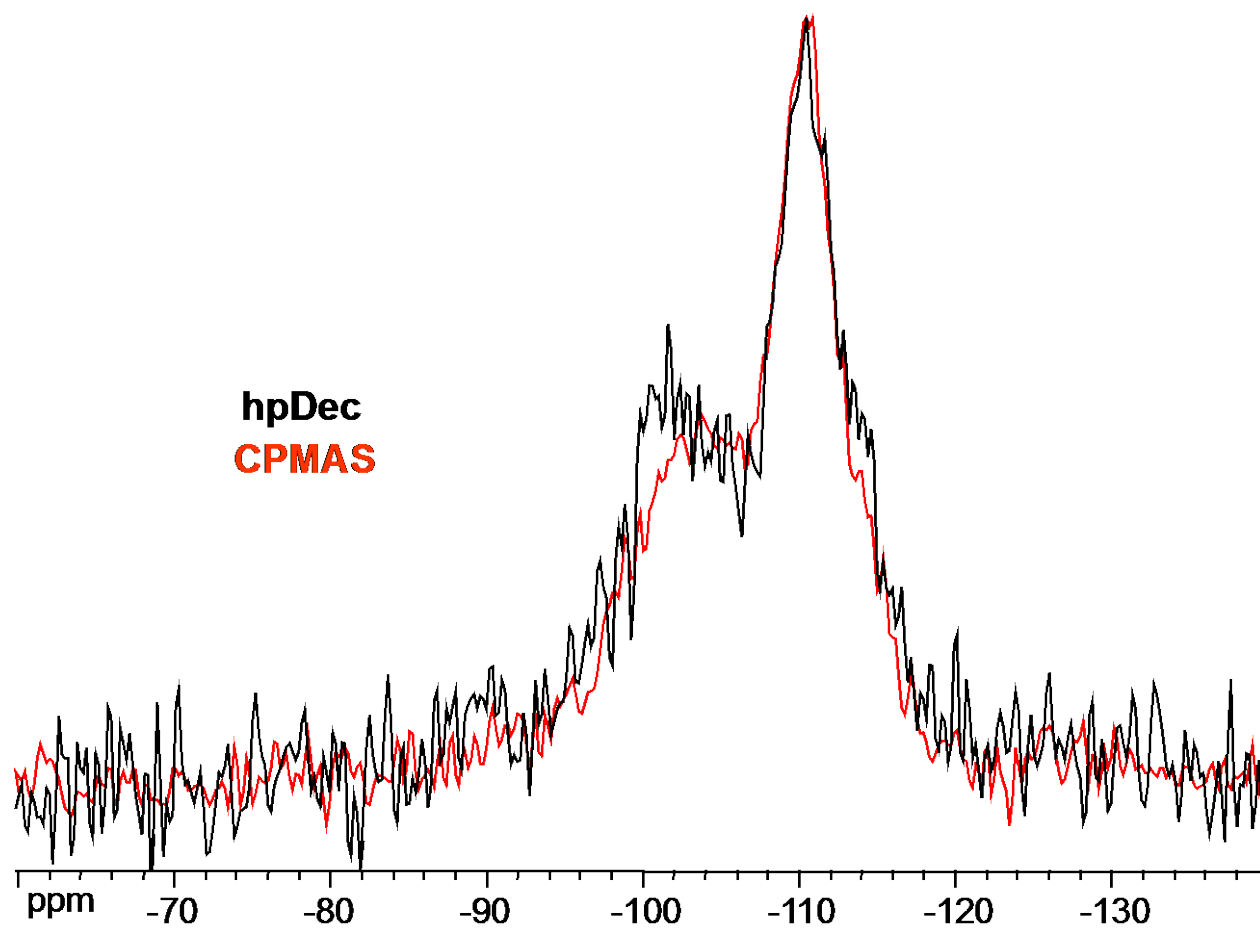


Figure S19. Comparison between direct polarization and cross-polarization $^{29}\text{Si}\{^1\text{H}\}$ MAS NMR spectra of as-synthesized nano-Beta_{gel} at 140°C for 3 days.

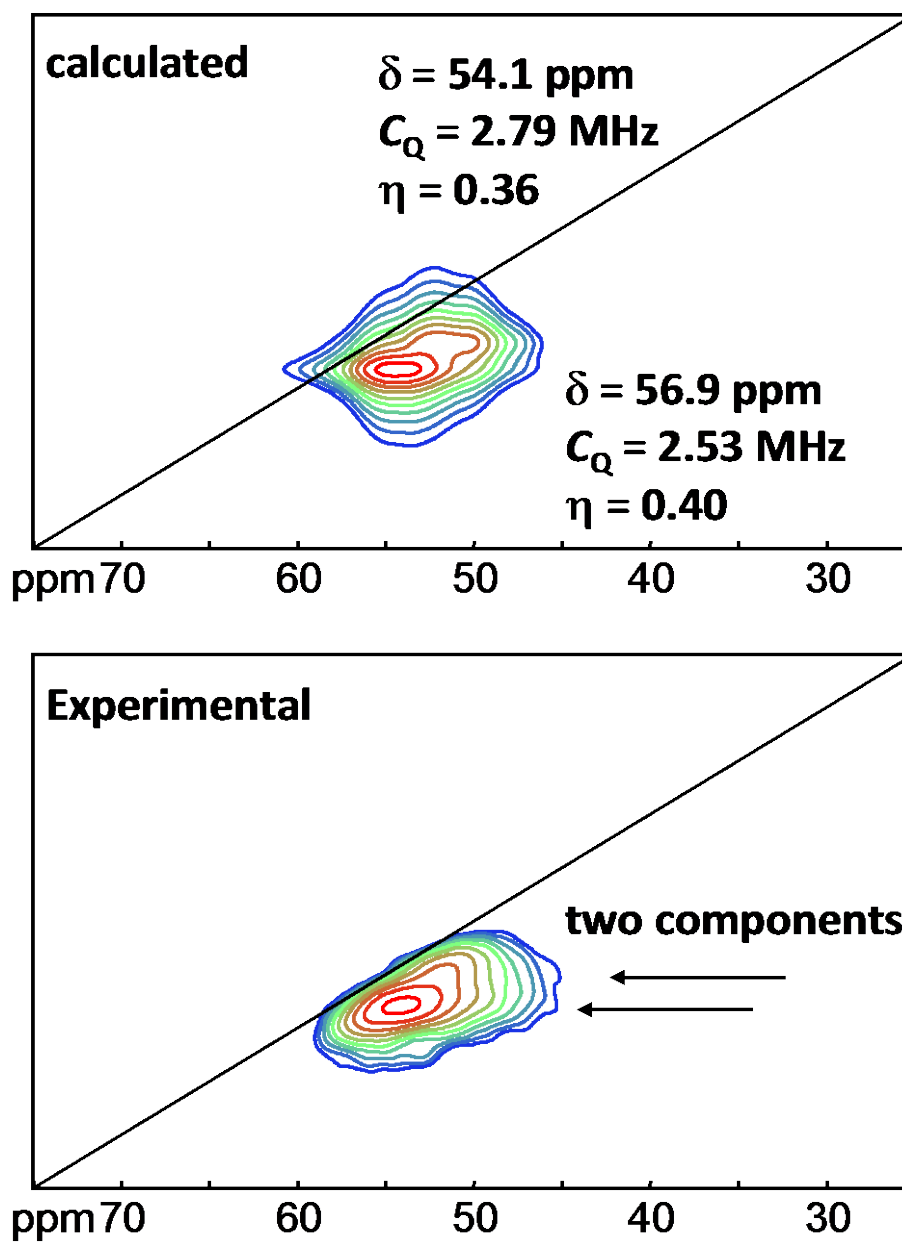


Figure S20. Experimental and simulated ^{27}Al 3QMAS spectra of as-synthesized nano-Beta_{sol} at 140°C for 22 days.

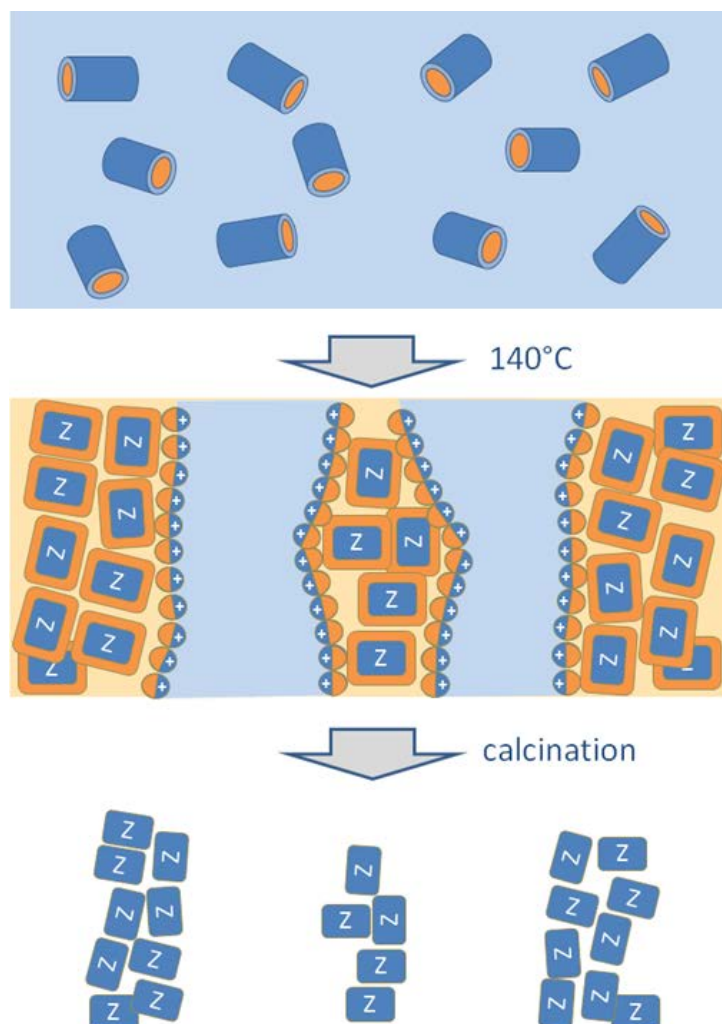


Figure S21. Synthesis of zeolite Beta crystallites from core-shell cylinders with inorganic shells. After formation of the zeolite, the crystallites are terminated by a hydrophobic coating. Spinodal decomposition-like mechanism results in two bi-continuous phases, i.e., an aqueous phase and an organic phase containing the zeolite. The boundary between the two phases can be stabilized by the amphiphilic SDA molecules. Evaporation of water causes the larger mesopores and decomposition of the organic phase via calcination causes aggregation of the zeolite nanoparticles by which smaller mesopores are formed as voids between particles.

Supplementary references

¹ Na, K.; Jo, C.; Kim, J.; Cho, K.; Jung, J.; Seo, Y.; Messinger, R. J.; Chmelka, B. F.; Ryoo, R. Directing Zeolite Structures into Hierarchically Nanoporous Architectures. *Science* **2011**, 333, 328–332.

² Kline, S.R. *J. Appl. Cryst.* **2006**, 39, 895–900.

³ <http://www.sasview.org/>

⁴ NMRNotebook, (<http://www.nmrtec.com/software/nmrnotebook>) from NMRTEC.

⁵ Phillips, J. C.; Braun, R.; Wang, W.; Gumbart, J.; Tajkhorshid, E.; Villa, E.; Chipot, C.; Skeel, R. D.; Kalé, L.; Schulten, K. Scalable Molecular Dynamics with NAMD. *Journal of Computational Chemistry* **2005**, 26, 1781–1802.

⁶ Vanommeslaeghe, K.; Hatcher, E.; Acharya, C.; Kundu, S.; Zhong, S.; Shim, J.; Darian, E.; Guvench, O.; Lopes, P.; Vorobyov, I.; Mackerell, A. D. CHARMM General Force Field: A Force Field for Drug-like Molecules Compatible with the CHARMM All-atom Additive Biological Force Fields. *Journal of Computational Chemistry* **2010**, 31, 671–690.

⁷ Van Gunsteren, W. F.; Daura, X.; Mark, A. E. Computation of Free Energy. *Helv. Chim. Acta* **2002**, 85, 3113–3129.